Geophysical Journal International

Geophys. J. Int. (2020) **223,** 1672–1687
Advance Access publication 2020 August 28
GJI Seismology

doi: 10.1093/gji/ggaa402

Seismic anisotropy in deforming halite: evidence from the Mahogany salt body

Philipp Prasse[1], James Wookey,[1] J-Michael Kendall,[2] Daniel Roberts[3] and Martin Dutko[3]

[1]*School of Earth Science, University of Bristol, Bristol, BS*81*RJ, United Kingdom. E-mail: philipp.prasse@gmail.com*
[2]*Department of Earth Sciences, University of Oxford, Oxford, OX*13*AN, United Kingdom*
[3]*Rockfield Global, Swansea Waterfront, SA*18*AS, Swansea, United Kingdom*

Received 2020 August 5; in original form 2020 February 17

SUMMARY

We present unambiguous evidence that the Mahogany salt body, located in the Northern part of the Gulf of Mexico, is seismically anisotropic. Evidence of anisotropy comes from shear wave splitting data obtained from a vertical seismic profile VSP. The data set consists of 48 vertically aligned receivers in a borehole drilled through the salt body. Splitting analysis is performed on shear wave phases that are converted from compressional waves at the top and bottom of the salt body. The phase converted at the top of the salt layer shows a clear signature of seismic anisotropy, while the phase at the base of the salt layer shows negligible splitting. We investigate the possibility of rock salt halite LPO as a cause of the observed anisotropy. A finite element geomechanical salt deformation model of the Mahogany salt body is developed, where deformation history is used as an input to the texture plasticity simulation program VPSC. Assuming a halite salt body, a full elasticity model is then calculated and used to create a synthetic VSP splitting data set. The comparison between the synthetic and real VSP data set shows that LPO of rock salt can explain the observed anisotropy remarkably well. This is the strongest evidence to date of seismic anisotropy in a deforming salt structure. Furthermore, for the first time, we are able to demonstrate clear evidence that deforming halite is the most likely cause of this anisotropy, combining data set analysis and synthetic full wave form modelling based on calculated rock salt elasticities. Neglecting anisotropy in seismic processing in salt settings could lead to potential imaging errors, for example the deformation models show an averaged delta parameter of $\delta = -0.06$, which would lead in a zero offset reflection setting to a depth mismatch of 6.2 per cent. Our work also show how observations of salt anisotropy can be used to probe characteristics of salt deformation.

Key words: Creep and deformation; Image processing; Numerical modelling; Seismic anisotropy.

1 INTRODUCTION

Since pre-Roman times salt has been of vital economic and cultural importance. Its special properties make salt crucial for a variety of historic and contemporary industrial applications. For example, geological salt formations are used for energy, compressed CO_2 and nuclear waste storage. Rock salt is also an important mineral in hydrocarbon reservoir settings. For example, the Luan Salt basin in the Gulf of Mexico is associated with significant oil and gas discoveries (Hudec & Jackson 2007). Understanding salt processes and dynamics affecting hydrocarbon reservoir production is important for their exploration and efficient exploitation. Such understanding requires accurate imaging of salt (and subsalt) structure, and there is a long history of seismic investigation of such settings (e.g. Hale *et al.* 1992; Lafond *et al.* 2003; Jackson & Lewis 2012). However, despite significant advances in sensor technology, compute availability and algorithms for seismic processing, it is still a common assumption to treat salt as seismically isotropic (e.g. Jones 2014, i.e. seismic velocity is invariant with propagation direction). If this assumption is not valid, seismic images based on it might be distorted (e.g. Alkhalifah *et al.* 1996). This can result in erroneous interpretations leading to, for example, costly drilling errors. In this study, we provide evidence that Mahogany salt body in the Gulf of Mexico is, in fact, significantly seismically anisotropic.

Salt has a low viscosity and density and is highly deformable but impermeable over geological timescales. It flows under tectonic forces if the deviatoric stresses are high enough. Salt is often the most deformable part of the sedimentary environment and has the

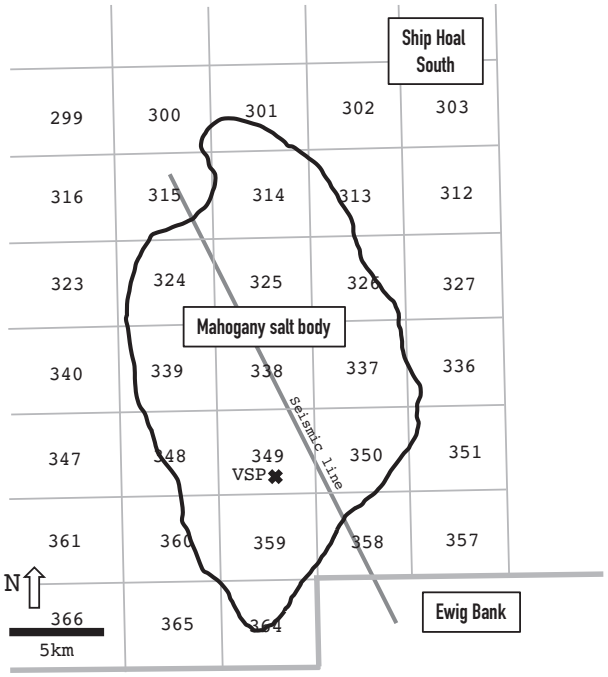

Figure 1. Location and dimension of the Mahogany salt body in a 2-D plan view is shown. The figure is modified from (Rowan *et al.* 2001). The Mahogany salt body is located in the South Ship Shoal area. The VSP well is at the South of Ship Shoal block 349. The Mahogany salt body has a dimension of about 15 km in east–west direction and about 30 km in north–south direction. The seismic line was used for seismic restoration, performed by (Rowan *et al.* 2001). A cross section along this line is shown in Fig. 2.

ability to flow rather than to fracture. It is relatively more buoyant than the surrounding sediments. The crystalline nature of salt—and its tendency to be highly deformed—means that it has the potential to manifest significant seismic anisotropy. Many polycrystalline materials develop texture (crystal or lattice-preferred orientation, LPO) and become seismically anisotropic when being deformed (for example, olivine; Hess 1964). As rock salt is a common polycrystalline solid, which is highly deformed in geological environments, it is reasonable to investigate its potential for seismic anisotropy due to crystal alignment. Halite has a cubic crystal structure and displays a significant elastic seismic anisotropy on single crystal scale (e.g. Zong *et al.* 2014; Vargas-Meleza *et al.* 2015) Thus, when subject to an overall alignment by crystal plastic deformation, salt may exhibit anisotropy at a scale relevant to seismic waves.

Some previous work on seismic anisotropy of salt suggests that despite the general assumption of isotropy, rock salt can display significant seismic anisotropy. Planchart (e.g. 2014) analysed salt anisotropy using a VSP from the Mansiyah salt formation, located in Saudi Arabia. By comparing seismic velocities at different offsets, the δ-parameter (Thomsen 1986) was estimated to be $\delta = -0.2$—a significant degree of anisotropy. Direct seismic velocity measurements were performed on pure rock salt samples from Sifto's Goderich Mine, Canada (Zong *et al.* 2014), showed a range in *P*-wave velocity from 4.44 to 4.76 km s^{-1}—a *P*-anisotropy of 6.9 per cent, ascribed to the cubic elastic anisotropy of the halite samples.

This study is motivated by Raymer et al. (2000b) who numerically investigated seismic anisotropy in deforming rock salt. They simulated halite LPO and seismic anisotropy under low temperature conditions for simple deformation regimes (simple shear and axial extension) by the use of dislocation plasticity models. The resulting fabrics show considerable degree of seismic anisotropy (up to 4 per cent *P*-wave anisotropy). However, the deformation regimes tested as well as the amount of strain were partly arbitrary and no comparison to a seismic data set were made. Here, we take a next step and take into account the complex deformation history of a salt structure. First, we investigate seismic anisotropy with a VSP data set, located in the Mahogany salt body, using shear-wave splitting (e.g. Silver & Chan 1991). Secondly, we develop a geomechanical salt sheet deformation model, simulating the deformation of the Mahogany salt body. Numerical texture plasticity models are then used to simulate LPO and seismic anisotropy by this lattice orientation. Finally, we compare the splitting determined from full-waveform synthetic seismograms interrogating this model to our observed results, showing that LPO of rock salt is a likely candidate to explain the observed anisotropy.

2 A VSP DATA SET OF THE MAHOGANY SALT BODY

The Mahogany oilfield is located in the northeast of the Gulf of Mexico, in the southern Ship Shoal area (block 349 and 359). The Mahogany salt body extends about 30 km in north–south direction and about 15 km east–west (Fig. 1). A cross section of the Mahogany salt body is shown in Fig. 2. Mahogany was discovered 1993 by the companies Phillips, Anadarko and Amoco (Weimer *et al.* 1998; Rowan *et al.* 2001; Harrison *et al.* 2010). Three years later in 1996, Mahogany became the first commercial subsalt oil reservoir in the Gulf of Mexico (Dribus *et al.* 2008). The field is a faulted anticline, forming a stratigraphic structural trap overlain by allochthonous salt (Camp 1998; Harrison *et al.* 2010). The subsalt reservoir is a highly pressured oil-saturated sand with high permeability and porosity dated around the upper Miocene (20 to 5 Myr, Rowan *et al.* 2001). The reservoir is below the large Mahogany salt sheet that converges with other salt structures neighbouring the salt body. Gross thickness of the oil-paying reservoir strata ranges from 30 to 107 m, below an approximately 1160-m-thick salt layer (Camp 1998). The large salt sheets pose technical (for example drilling) and seismic challenges, due to its pressure and velocity contrast to the surrounding sediments. Most seismic energy is reflected at the top of the salt, which makes subsalt imaging difficult.

2.1 VSP structure and geometry

The seismic data presented is obtained from a VSP data set located in the Mahogany oil field, in the South of Ship Shoal block 349 (Fig. 1). The three-component receivers of the VSP are aligned inside the subsalt well, consisting of 48 receivers, with a spacing of 15 m between each receiver. The upper 10 receivers are in the salt and the lower 38 receivers are located in the shale beneath the rock salt layer. The first receiver is at a depth of about 3540 m. The source is a single, long-offset source, located northeast of the borehole. Because of the distant source, strong wave conversions are seen from both the top and base of the salt. The distance from the source to the receiver is about 6 km. This is a good geometry for studying anisotropy in the salt body: the offset VSP provides long travel paths through the salt (providing the opportunity to accrue anisotropic effects) while the one way nature of the propagation reduces possible attenuation problems. The traveltimes should also not be strongly affected by invaded zones due to drilling processes

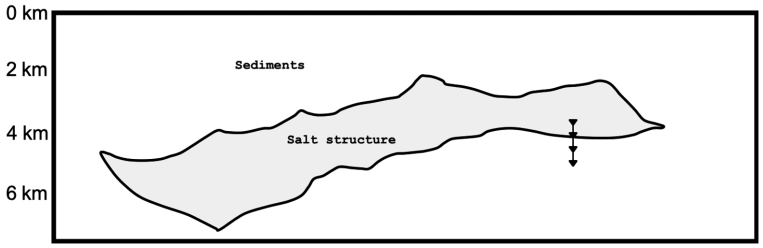

Figure 2. 2-D Cross section of the Mahogany salt body. The cross section was generated by seismic restoration along the seismic line shown in Fig. 1. Salt is shown in grey. The picture is redrawn from Rowan *et al.* (2001) showing the 2-D geometry of the Mahogany salt body along the seismic line, where the left-hand side is the NNW end of the seismic line and the right-hand side is the SSE end. The VSP location is shown at the right-hand side of the salt body.

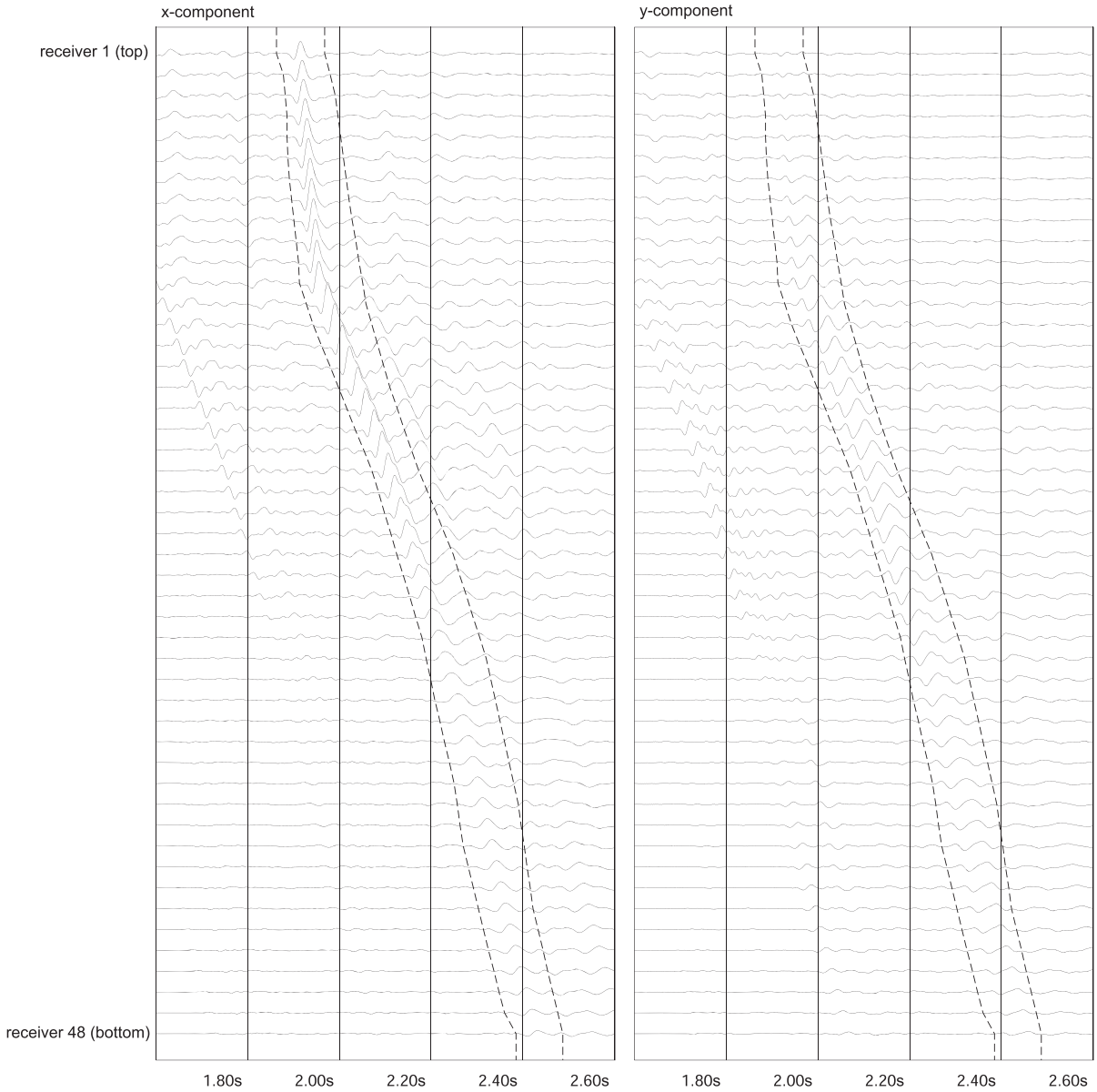

Figure 3. The original VSP data, recorded on the two horizontal components (x and y). In the left-hand panel shows the x-component, the right-hand panel shows the y-component.

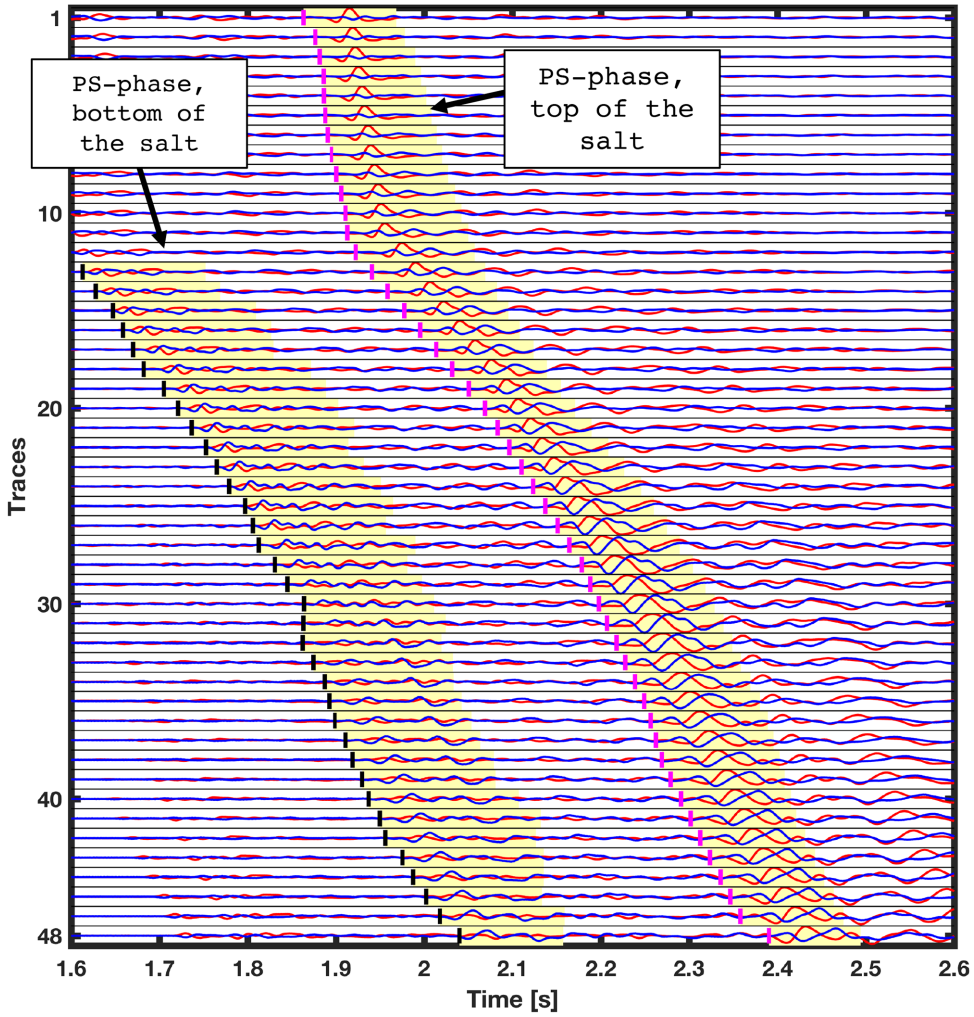

Figure 4. Filtered VSP data for all 48 receivers, where receiver 1 is the shallowest top and receiver 48 is the deepest. The *X*- (radial) and *Y*-component (transverse) are shown in red and blue, respectively, for each receiver. The receivers within the salt (traces 1–10) show higher velocities than the receivers below the salt (traces 11–48). The picked *PS*-phases, converted at the top of the salt and bottom of the salt are highlighted for each receiver.

near the borehole. We measure shear wave splitting in *P*–*S* conversions at both the top and base of the salt. This allows us to study seismic anisotropy in the salt body itself, without being contaminated by anisotropy in either the over- or underlying sediments.

2.2 VSP data preparation

The data discussed here were originally presented, processed and analysed by Kendall *et al.* (1998). The original data we received is shown in Fig. 3. The *X*- and *Y*-component is shown, unfortunately we do not have access to the vertical component. The data were processed to isolate (as best as possible) downgoing shear wave energy. The up- and downgoing *P*- and *S*-wave arrivals were identified in the data, and the wavefields were separated using a *f*–*k* filter (e.g. Christie *et al.* 1983; Sheriff & Geldart 1995). In the *f*–*k* domain, the different apparent velocities of up- and downgoing shear waves are used to distinguish the different phases. Extraneous arrivals were then removed by the use of the *f*–*k* filter. Finally, the data were then restored to their original position. This is the format we received the data in, no access was possible to the original raw data. The methodology used to obtain the results was not documented. Here, we re-analyse these data, and use up to date, robust analysis methods for measuring seismic anisotropy and shear wave splitting (Wuestefeld *et al.* 2010).

The final, filtered VSP-data are shown in Fig. 4. The *X*- (transverse) and *Y*-components (radial) are shown in red and blue, respectively. Both *PS*-phases, on which the shear wave splitting measurements are performed, are highlighted. The phases were picked by hand. Our aim is to analyse seismic anisotropy in the salt: The *PS* top-salt conversion will show shear wave splitting associated with both the rock salt and layers below. The *PS* base-salt conversion should only be affected by anisotropy beneath the salt. Thus, the difference constrains the splitting associated with the salt body.

We estimate splitting parameters (delay time, dt, and fast shear wave polarization, Φ) for the VSP field data set on all traces. The angle of fast shear wave polarization is measured in degrees as the clockwise angle from the direction of the radial component when looking along the downgoing vertical (Z-component) towards the origin (fast shear wave polarizations close $\pm 90^\circ$ means $V_{SH} > V_{SV}$). We perform shear wave splitting analysis on two phases: The *P* to *S* converted waves at the top, and base of the salt body, respectively. The difference between these constrains the seismic anisotropy originating from the rock salt. Shear wave splitting measurements are performed with SHEBA (Wuestefeld *et al.* 2010), which is built

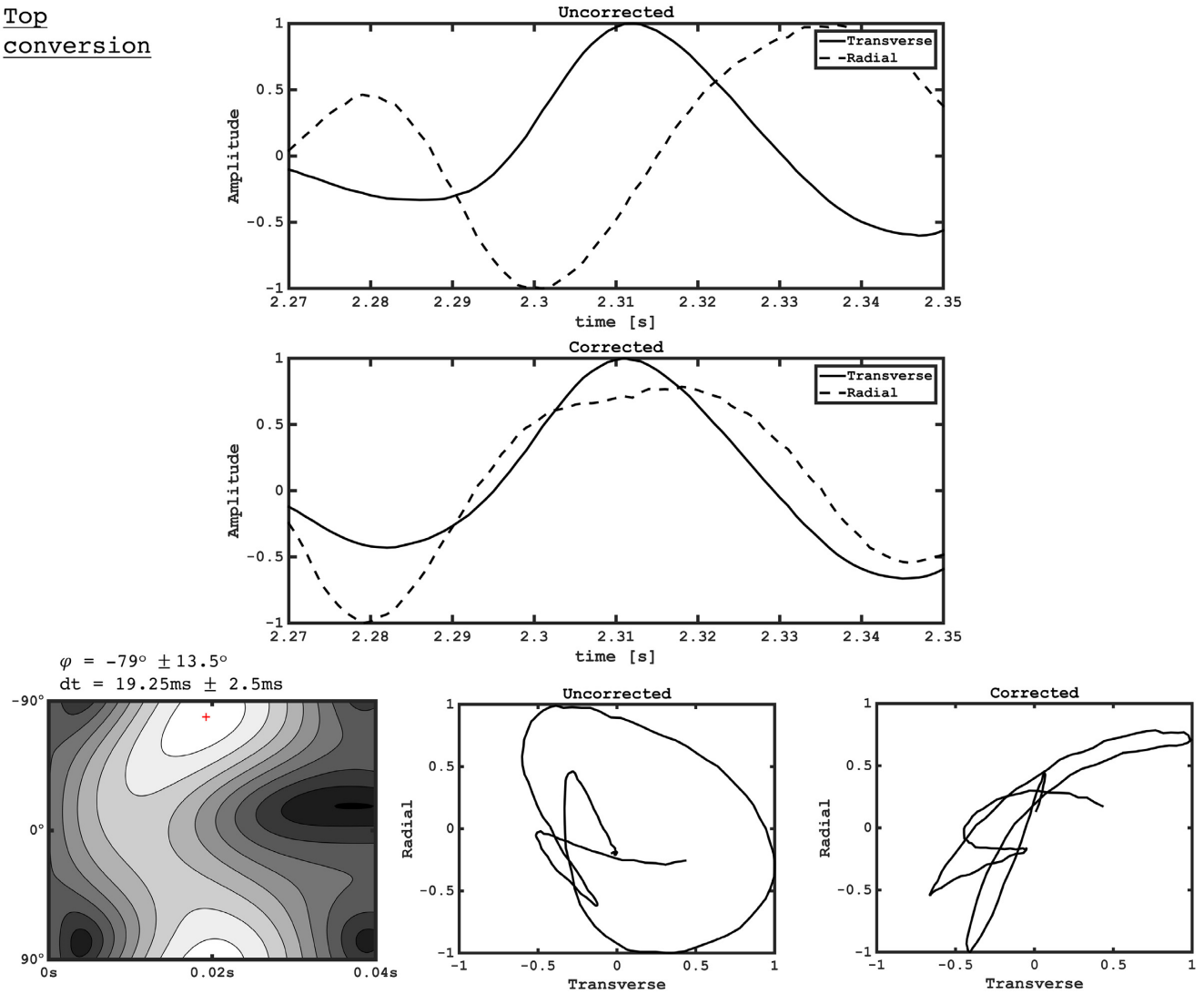

Figure 5. Sample shear wave splitting results from receiver 37 from the *PS*-top converted wave. Shown are the uncorrected and the corrected traces and the related particle motion. In the uncorrected case, the traces are separated by a time delay d*t* and the particle motion is elliptical. In the corrected case, the traces do not show a time delay and the particle motion is linear, because the splitting is removed, and energy is only polarized in one direction. The error-surface of the eigenvalue-method is shown, and indicates a high degree of confidence in the result.

on the seismic analysis code (SAC) platform (e.g. Helffrich *et al.* 2013). The splitting parameters are found by rotating the components from radial- and transverse into fast- and slow-direction, using the eigenvalue- and cross correlation method (e.g. Wuestefeld & Bokelmann 2007). For each measurement, the best splitting results are found from 100 candidate windows. We also estimate Q, the shear wave splitting quality (Teanby *et al.* 2004; Wuestefeld & Bokelmann 2007). This allows us to assess the robustness of the result. A shear wave splitting example of receiver 37 from the top- and bottom converted *PS*-wave is shown in Figs 5 and 6, respectively.

2.3 Shear wave splitting results

Time delay d*t* and fast shear wave polarization Φ of the top- and bottom converted shear waves are shown in Figs 7 and 8, respectively. The error bars indicate the 95 per cent confidence level in each measurement (Silver & Chan 1991). Both the top- and base *PS*-conversions show evidence of splitting. However, the top-conversion shows consistently significantly higher delay times than the base-converted phase (15–20 ms compared to 4–8 ms). The delay time of the top-converted phase increases with increasing receiver depth, until the receivers are outside of the salt. After receiver 25, the delay time is very consistent around 18 ms. The delay time depends on the traveltime, and incidence angle of the incoming wave to the receiver. Receiver 11–18 show high delay times (and associated error) and are marked on Fig. 7 by a red area indicating where wave-conversions at the salt/sediment boundary may affect the splitting measurements. For example, we can expect a degree of *S–P* phase conversion at the base salt, which might not be entirely removed by the applied *f–k* filter. If we discount these results the delay time generally increases with depth within the salt and remains approximately stable at around 20 ms below receiver 20. The best constrained results are from the receivers which are well outside of the salt (receiver 32–48). These have a constantly high quality, low error and give similar and consistent delay times. The base-converted shear waves shows evidence of splitting, but the magnitude is significantly less, and the Q-values are lower. This suggests that the splitting observed at the

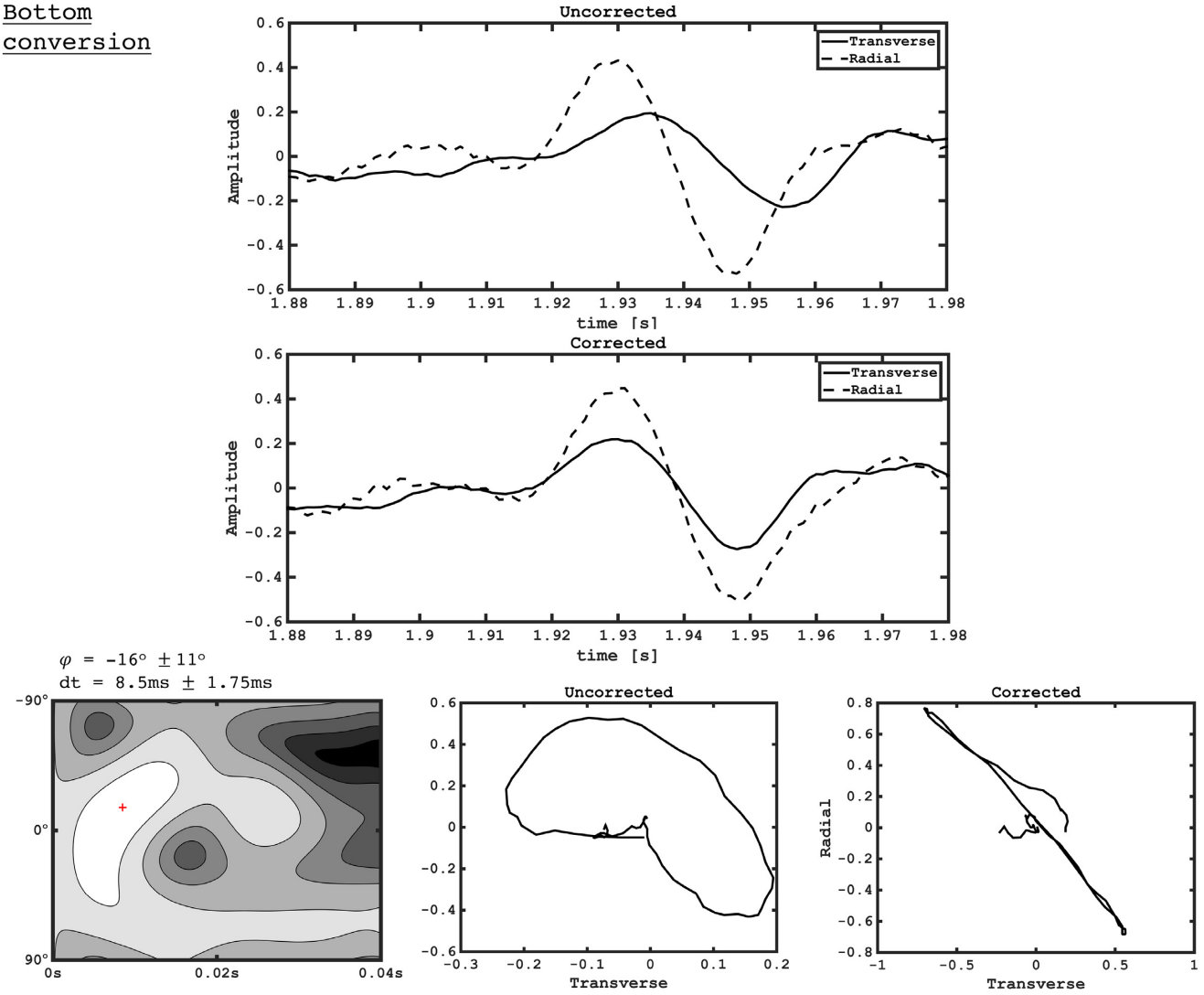

Figure 6. Sample shear wave splitting results from receiver 37 from the *PS*-bottom converted wave (same receiver as in Fig. 5). Shown are the uncorrected and the corrected traces and the related particle motion. In the uncorrected case, the traces are separated by a time delay d*t* and the particle motion is elliptical. In the corrected case, the traces do not show a time delay and the particle motion is linear, because the splitting is removed, and energy is only polarized in one direction. The error-surface of the eigenvalue is shown.

top-converted shear wave originate in the salt. The fast shear wave polarization of the top-converted phase shows a fast shear wave polarization around ±90° (Fig. 8a). This would correspond, in the simplest case, to a VTI-medium. The bottom-converted shear wave, on the other hand, shows a fast polarization close to 0° (Fig. 8b), which would correspond to a HTI medium. The results show strong evidence that the Mahogany salt body, for the investigated acquisition and geometry, is seismically anisotropic.

3 NUMERICAL TEXTURE MODELLING

In following we investigate if the deformation of the Mahogany salt can lead to effective LPO and consequently seismic anisotropy. We investigate the simplest case of this anisotropy, LPO of halite. To do this, we need to model the formation of crystal fabric under realistic deformation conditions. We perform texture simulations with the viscoplastic self-consistent texture modelling approach (VPSC, Lebensohn & Tomé 1993). VPSC has been successfully used to model deformation textures of halite, in various deformation setups, as for example simple shear (Wenk *et al.* 2009), extension (Wenk *et al.* 1989; Lebensohn *et al.* 2003) and compression (Lebensohn *et al.* 2003). Moreover, it was used to model deformation texture of naturally deformed rock salt (Raymer *et al.* 2000b, a). Therefore, it is reasonable to use texture plasticity modelling in more complex, and realistic deformation regimes.

3.1 Viscoplastic self consistent—VPSC

The VPSC approach can model a range of conditions, from the homogeneous deformation assumption (Taylor model) to the stress equilibrium assumption (Sachs model, e.g. Wenk *et al.* 2009). The averaged stress predicted by VPSC is placed somewhere between the predictions by the upper-bound Taylor model and lower-bound Sachs model. A detailed description can be found in Tomé *et al.* (1991) and Lebensohn & Tomé (1993); here we briefly summarize the approach and its main principles. The shear rate $\dot{\gamma}^s$ of a slip system s in an individual grain is assumed to be related to the

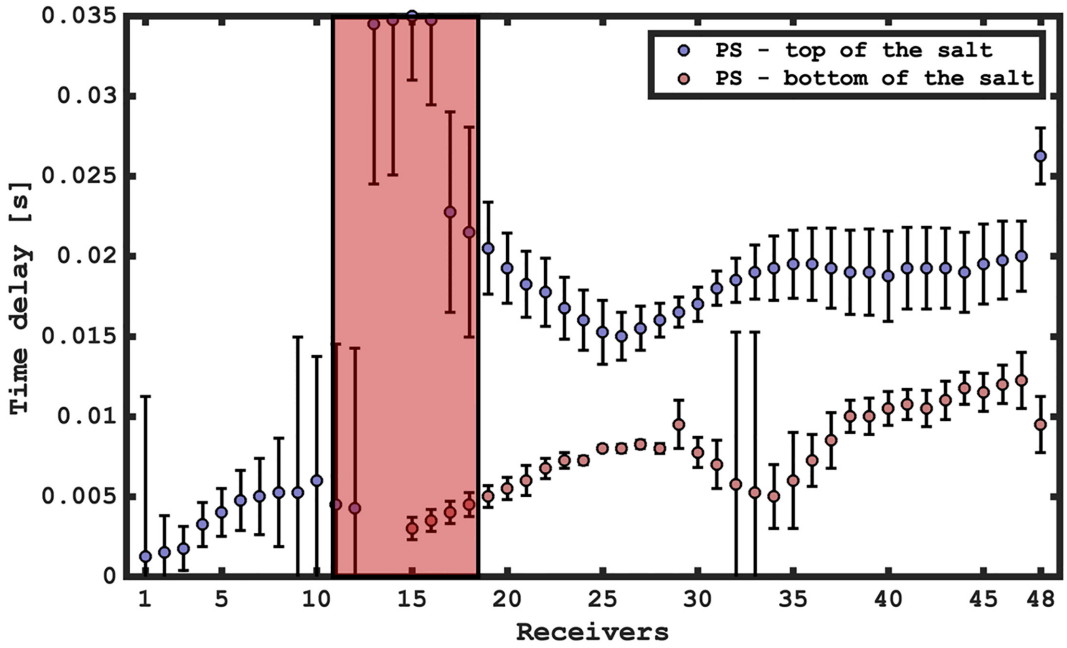

Figure 7. Comparison of the delay times from the *P*- to *S*-converted phase at the top of the salt layer (shown in blue) and the bottom of the salt layer (shown in red). The red region mark receivers close to the salt/sediment boundary, which might be affected by wave-conversions in the splitting window. The top converted phase shows significantly higher delay times than the bottom converted phase. The delay time of the top-converted shear wave shows an increasing delay time with receiver depth. This indicates clear seismic anisotropy in the salt layer.

resolved shear stress τ_r^s in the following way:

$$\dot{\gamma}^s = \left(\frac{\tau_r^s}{\tau_0^s}\right)^n \dot{\gamma}_0, \tag{1}$$

where $\dot{\gamma}_0$ and τ_0^s are the reference shear rate and the reference CRSS, respectively. The grain's shear rate $\dot{\epsilon}$ is then given by the sum of shear rates over all slip systems. The stress exponent is n, which is the inverse of the strain rate sensitivity. For a given set of reference shear stresses and stress exponents for all active slip systems, initial lattice orientations and the imposed deformation. VPSC calculates the microscopic stresses and strain rates for each grain $(\sigma, \dot{\epsilon})$ (Tommasi *et al.* 2000).

Interaction between grains is represented by embedding each grain in a homogeneous effective medium (HEM). Its properties are the averaged properties of all modelled single crystal grains. The tangent VPSC method uses a more general model description (Lebensohn & Tomé 1993), which incorporates a formulation for a plastically anisotropic HEM. The interaction problem is solved using the inclusion formalism, described by Eshelby (1957). The local variables (stress σ_{ij} and strain ϵ_{ij}) on a grain scale are related to the same variables on the global scale (Γ_{ij}, E_{ij}) with the interaction tensor M, which depends on the shape and the rheological properties of grains. For the viscoplastic inclusion problem, the Eshelby solution is (e.g. Walker *et al.* 2011):

$$\dot{\epsilon_{ij}} - \dot{E_{ij}} = -\alpha M_{ijkl}\left(\sigma_{kl} - \Gamma_{kl}\right), \tag{2}$$

where α is a parameter controlling the interaction between the grains and the HEM, for example to impose more or less strict kinematic conditions on grains (Tommasi *et al.* 2000). The tangent VPSC scheme applied in this work assumes $\alpha = 1$. The lattice rotation rate for each grain $\dot{\omega}$ is determined by:

$$\dot{\omega}_{ij} = \dot{\Omega}_{ij} - \dot{\omega}_{ij}^p + \tilde{\omega}_{ij}, \tag{3}$$

where Ω is the antisymmetric component of the imposed deformation, $\dot{\omega}_{ij}^p$ is the plastic rotation rate tensor and $\tilde{\omega}_{ij}$ describes the reorientation rate of the associated ellipsoidal inclusion. The reorientation rate depends on the difference between the grain and polycrystal strain rate, increasing with increasing deformation. The VPSC model calculates the crystallographic texture, the activity of the slip systems and the stress/strain response of the polycrystal during the deformation. Required inputs are the initial grain shape and orientation, slip systems and their critical resolved shear stresses, single crystal properties (density and the elasticity tensor), the applied deformation and numerical parameters controlling the convergence and precision of each simulation.

In the modelling the CRSS are relative values, normalized by the strength of the weakest slip system. We use a CRSS ratio of 1:5:5, which means that {110}<110> has a CRSS 5 times lower than {100}<110> and {111}<110>, which implying low temperature deformation conditions (Wenk *et al.* 1989; Picard *et al.* 2018). In many numerical, and schematic models of salt diapirism, the salt diapir reaches the surface and is extruded at the surface as a salt sheet (e.g. Van Keken *et al.* 1993; Rowan *et al.* 2001; Hudec & Jackson 2007), suggesting low temperature deformation. Stress exponents used in flow laws for natural rock salt vary between 4 and 6 (Heege *et al.* 2005). Therefore, we suggest that an input parameter set of 1:5:5 for the CRSS-ratio and a stress exponent of $n = 6$ are best to represent natural deformation conditions. This is in the range of what has been used by Raymer *et al.* (2000b) to model texture in naturally deformed rock salt. The slip systems (from Carter & Hansen 1983) and the CRSS used in this study are shown in Table 1.

We use the Von-Mises stress Γ^{VM} and Von-Mises strain rate $\dot{E}^{\mathrm{VM}}$ to quantify the deformation (described in Hosford 2010). The Von-Mises strain is a function of the macroscopic stress and strain rate tensors (Γ_{ij} and $\dot{E}_{ij}$, respectively), representing the global stress and

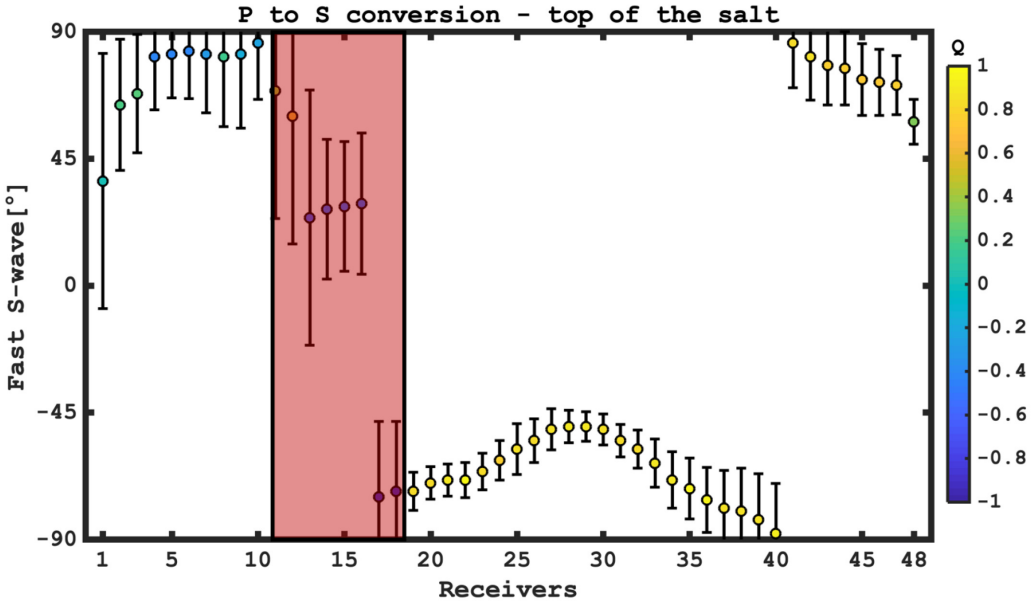

(a) Fast shear-wave polarisation and Q-value for the 48 receivers of the PS-top converted shear wave.

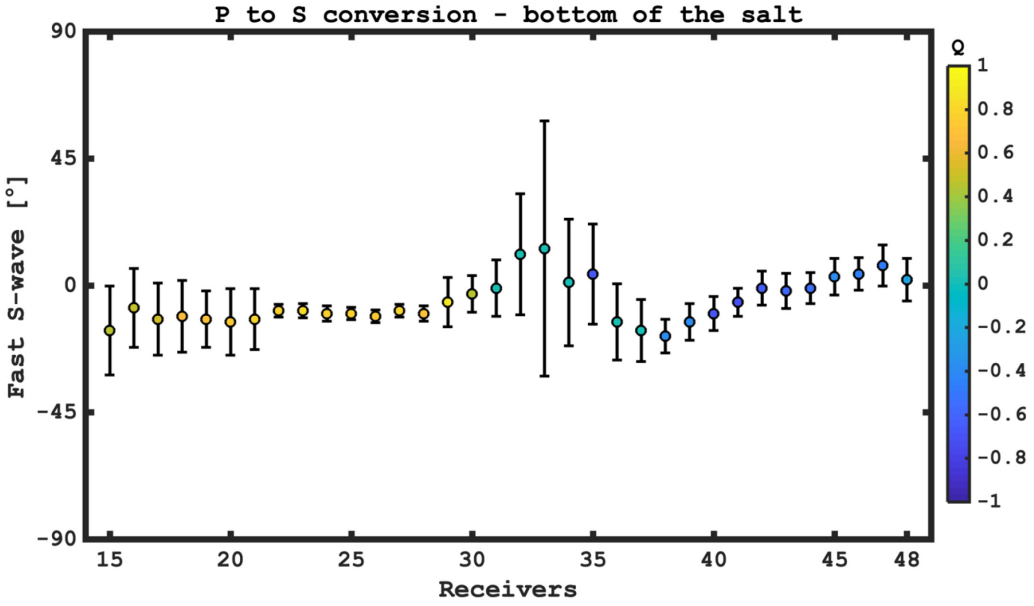

(b) Fast shear-wave polarisation and Q-value for the PS-base converted shear wave at receiver 15-48.

Figure 8. Fast shear wave polarization from the *PS*-top (a) and *PS*-bottom (b) converted phase. The colour represents the Q-value (–1: perfectly resolved null, +1:perfectly resolved splitting). Receivers, which are affected by wave conversions at the salt/sediment boundary are shown by the red region. The top converted shear wave (a) shows a fast polarization around $\pm 90^\circ$, which would suggest a VTI medium. The data shows good quality and high Q-values. The bottom converted shear wave (b) shows a fast polarization around 0° and low Q-values. The results suggest that the splitting originate in the salt body, meaning that the Mahogany salt body is seismically anisotropic.

strain state in the following way:

$$\Gamma^{VM} = \sqrt{\frac{3}{2}\Gamma'_{ij}\Gamma'_{ij}},$$
$$\dot{E}^{VM} = \sqrt{\frac{2}{3}\dot{E}_{ij}\dot{E}_{ij}}. \quad (4)$$

3.2 Finite element deformation model

We simulate the geological evolution of a near-surface salt body into an advancing salt sheet, in a compressional tectonic regime in 2-D, based on the deformation of the Mahogany salt body. The model is used to calculate deformation texture of halite inside the model during deformation. Deformation is interposed with sedimentation of new material. The model is a plane-strain, forward finite-element model, with adaptive remeshing, to cope with large deformation (Perić & Crook 2004). The simulation and model building are done

Table 1. Slip systems and slip modes being active in single crystalline halite: {110}⟨110⟩ is the weakest slip system; {100}⟨110⟩ and {111}⟨110⟩ are more difficult to activate. From Carter & Hansen (1983). CRSS of 1:5:5 are used for the weak, and stiff slip system, respectively. A stress exponent of 6 is used for all slip systems.

Slip system	Number of slip modes	Slip plane	Slip direction	CRSS	n
{110}⟨110⟩	6	1 1 0	1–1 0	1	6
		–1 1 0	1 1 0		
		1 0 1	1 0–1		
		1 0 –1	1 0 1		
		0 1 1	0 1 –1		
		0 1 –1	0 1 1		
{100}⟨110⟩	6	1 0 0	0 1 1	5	6
		1 0 0	0 1–1		
		0 1 0	1 0–1		
		0 1 0	–1 0 1		
		0 0 1	1–1 0		
		0 0 1	–1 1 0		
{111}⟨110⟩	12	1 1 1	1–1 0	5	6
		1 1 1	1 0–1		
		1 1 1	0 1–1		
		–1 1 1	0 1–1		
		–1 1 1	1 0 1		
		–1 1 1	1 1 0		
		1–1 1	0 1 1		
		1–1 1	1 0–1		
		1–1 1	1 1 0		
		–1–1 1	0 1 1		
		–1–1 1	1 0 1		
		–1–1 1	1–1 0		

with the geomechanical modelling software Elfen, developed by the software company Rockfield Global. We limit the model to two dimensions, which is sufficient to capture the primary deformation at Mahogany. A 2-D model also improves the computational tractability.

Our model consists of two materials, salt and sediments. The rheology of the salt is represented by the multimechanism deformation (MD) constitutive model. It is a mathematical formulation describing the mechanical creep behaviour of various rock salts. It takes into account dislocation climb, dislocation creep and a third undefined mechanism. The formulation of the MD rheology model was first presented in Munson & Dawson (1979) and has been used extensively to model creep behaviour of rock salt. It has been applied to various rock salt deposits around the world, for example to Brazilian salts (Firme *et al.* 2015) or to salts from the Gulf coast (e.g. Munson *et al.* 2004; Fredrich *et al.* 2007; Thigpen *et al.* 2019). The salt density is assumed to be $\rho_{\mathrm{Salt}} = 2.1\ \mathrm{g\,cm^{-3}}$. The sediments are modelled by the SR3 material model (Crook *et al.* 2006). The SR3 material model is a constitutive critical-state poroelastic-plastic material model, based on the 'cam clay' material model concept (Wood 1990). The bulk density of the sediment is defined based on assumed grain and fluid densities and the current element porosity. Therefore, as the material state evolves due to burial and tectonics the bulk density is updated accordingly. All parameters used for the model are shown in the Appendix.

The model initial geometry and the evolution of the conceptual model are shown in Fig. 9. The salt has an initial extension of about 5 km × 4 km, representing a salt diapir which has penetrated the upper sedimentary layers and reached the surface. The applied tectonic stress is solely compression from the left-hand side of the model with a shortening rate of 1 mm yr^{-1}. The right-hand side of the model is fixed. 5.9 Myr of deformation time is modelled, while new material is deposited along with deformation. The sedimentation is modelled by progressively adding new material on top until predefined horizons are reached. The horizons have a slight angle basinward, imitating progessive sedimentation. The sedimentation rate is about 0.6 mm yr^{-1}, slightly lower than the compression rate. After the deformation completes, the geometry of the salt sheet is close to the 2-D-cross section of the Mahogany salt body, shown in Fig. 2.

3.3 Elasticity calculations

VPSC plasticity modelling is used to calculate texture evolution during the deformation. For this, 512 passive tracer particles are followed through the Mahogany salt sheet model in time. At each time step (every 0.1 Myr), the deformation velocity gradient tensor L of each particle is calculated. It is defined as the change of the deformation velocity with direction and defines the applied deformation entirely. This contains information about both the strain- and rotation-rate (Munson *et al.* 2013) and is used as an input for the texture plasticity modelling.

Each particle represents one halite polycrystal consisting of an initial set of 500 randomly oriented grains. Due to its random orientation the polycrystal shows no seismic anisotropy before it is being deformed. Grains are treated as ellipsoidal inclusions. In their initial undeformed stage, each has a spherical axis aspect ratio of 1:1:1. Each crystal has the properties of a halite single crystal. The elastic properties of halite hve been analysed in various studies; we take the single crystal stiffness tensor and the density from Gebrande (1982), which are $C_{12} = 14$ GPa, $C_{11} = 49.1$ GPa, $C_{44} = 12.7$ GPa and a density of $\rho = 2160\ \mathrm{kg\ m^{-3}}$. After deformation, effective elastic constants of each polycrystal are calculated, which can be seen as an average across all stiffness tensors c_{ijkl}, it has 21 independent constants and can rewritten in the Voigt notation as a 6 × 6 tensor

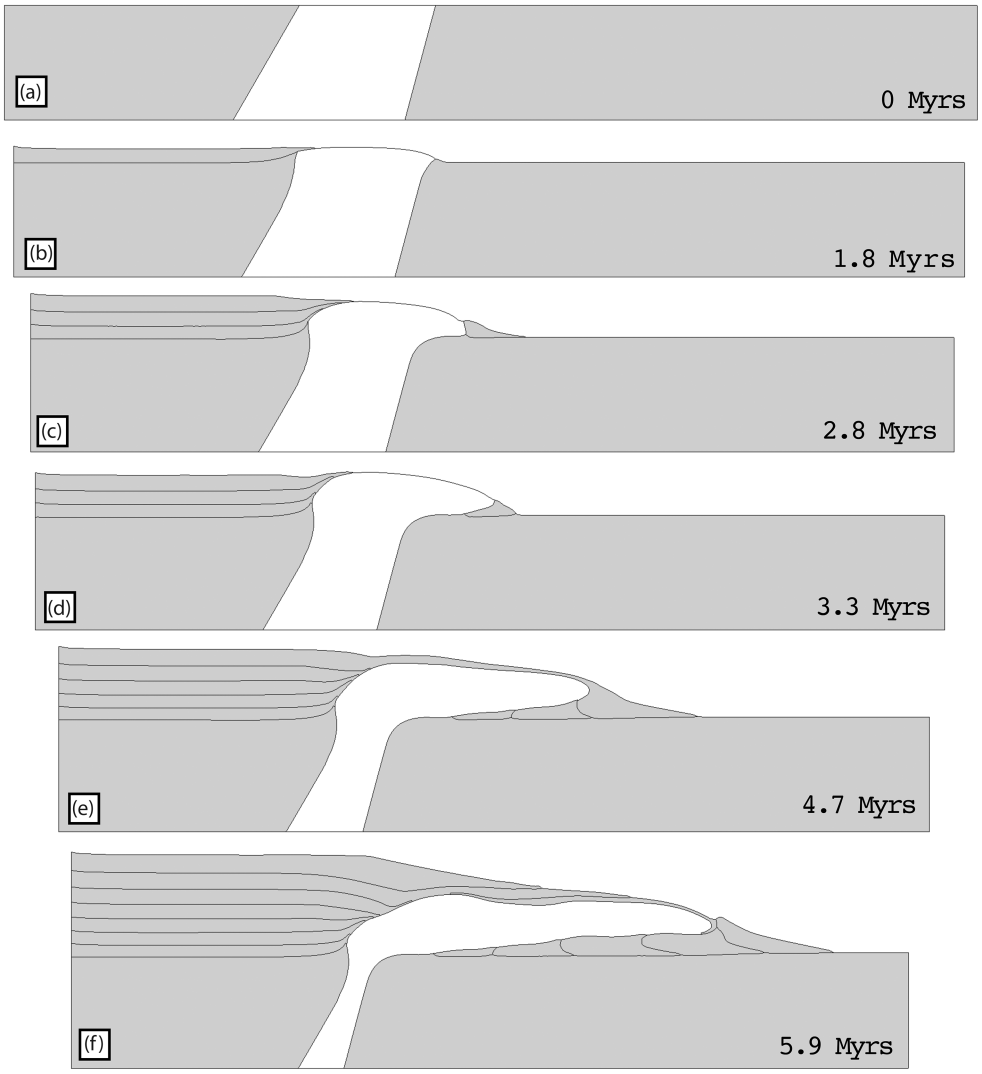

Figure 9. A finite-element (Elfen) model simulating the transition from a near-surface salt body into an advancing salt sheet. The salt sheet geometry is based on the present size of the Mahogany salt sheet in the Gulf of Mexico, modelled for 5.9 Myr. Panel (a) shows the initial geometry. Sediments are deposited and the salt sheet starts to extrude at the surface (panel b). At 2.8 Myr sediments are deposited in the front of the salt sheet (c). The base of the salt ramps up, non-parallel to the bedding plane (d). This process continues with ongoing time and deposition (e). At 5.9 Myr the salt sheet is thinned towards the basin and has an extension to about 15 km (f).

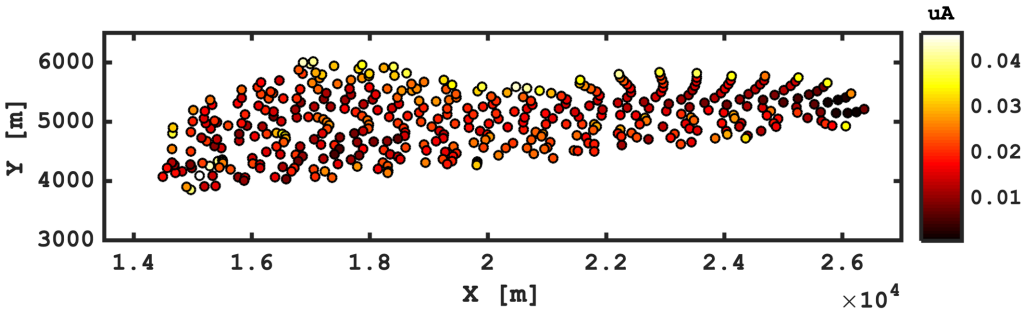

Figure 10. Seismic anisotropy inside the Mahogany salt sheet model. Seismic anisotropy is given as the universal-anisotropy index (Ranganathan & Ostoja-Starzewski 2008)), larger values indicating higher anisotropy. The salt from the diapir is pushed at the surface and rafts along the base, where large strain accumulates. The salt sheet is thinned towards the basin. The top- and base of the salt sheet shows generally higher anisotropy.

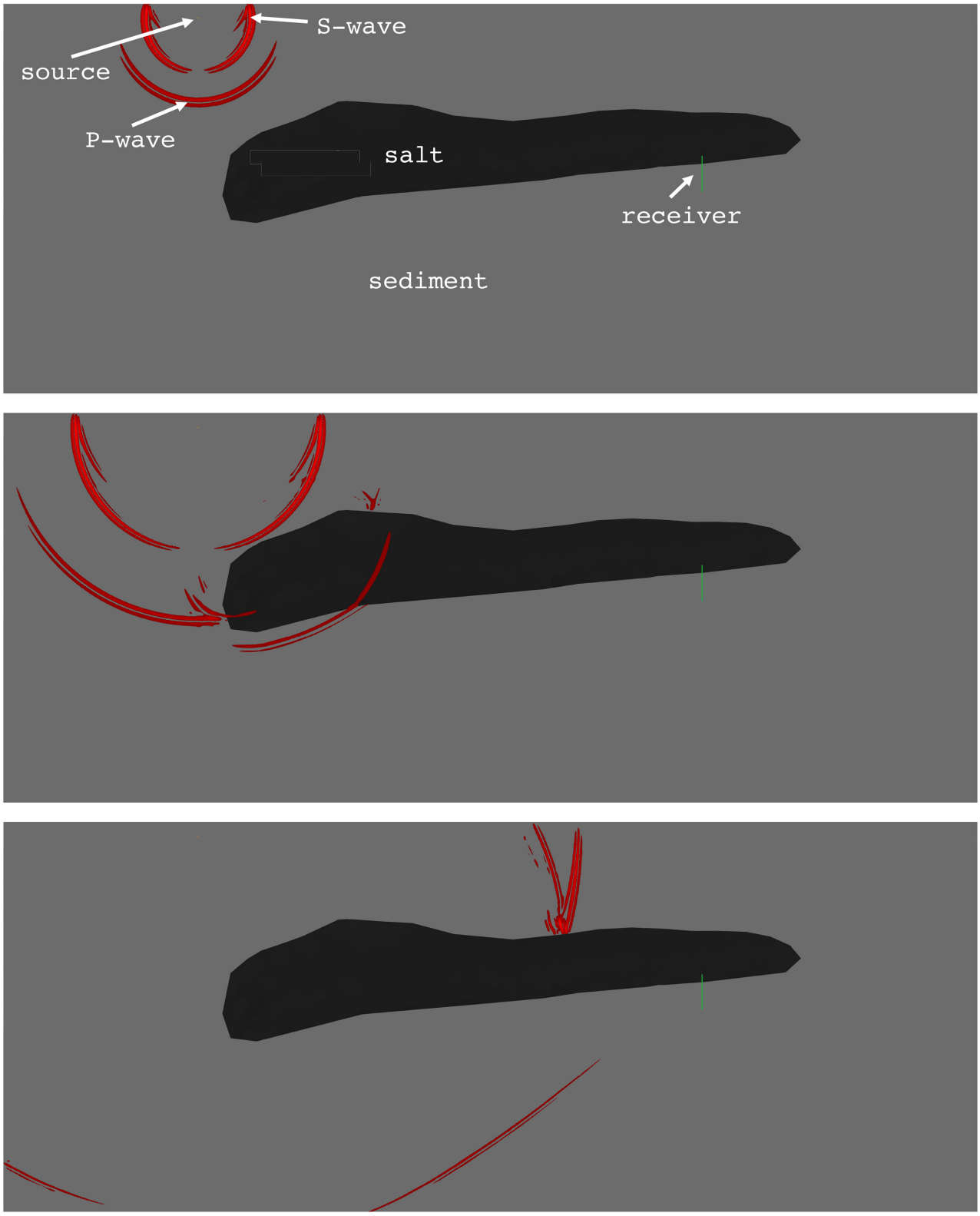

Figure 11. Wave propagation through the Mahogany model. The 48 receivers are shown in green and are located at the bottom right-hand end of the salt body. The seismic waves are shown in red and display the displacement normalized to the highest amplitude in each time step. The source is at the left-hand side of the model near the surface. The wave field is shown at 0.8, 1.7 and 5 s. The *P* wave and *S* wave are marked in the first snapshot at 0.8 s. The model consists of two phases, the isotropic sediment and the anisotropic salt. The model setup should mimics the VSP data set from the Mahogany salt body.

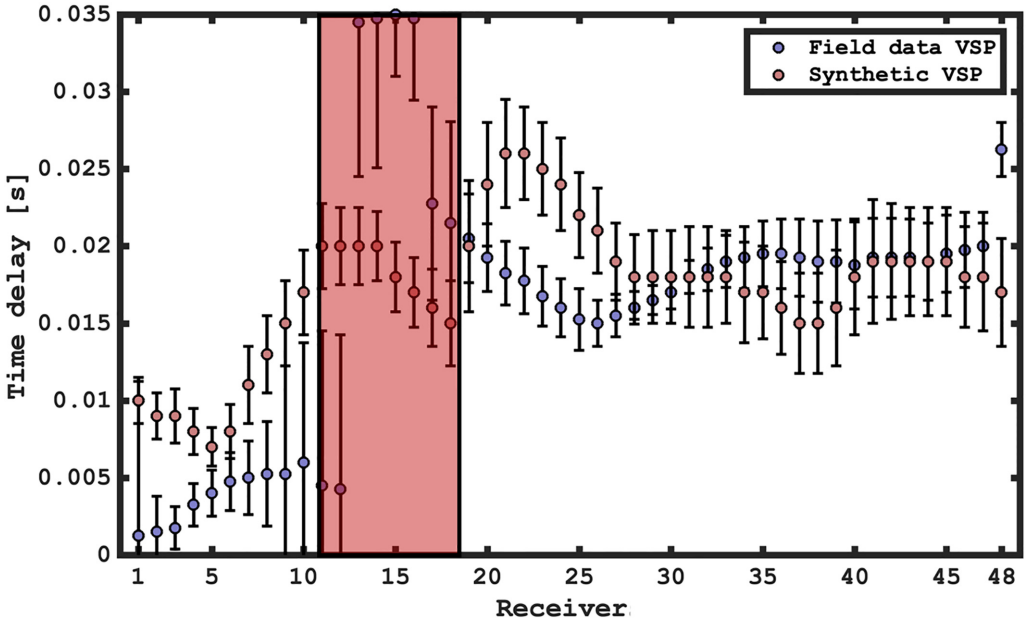

Figure 12. Comparison between the delay occurring in the synthetic data and the VSP field data. Field data delay times are shown in blue, synthetics in red. In general these agree well, especially beyond receiver 25, where both predict a delay time of about 20 ms. The region, in which we infer interference from the salt-sediment boundary is marked by the red bar.

($ij \rightarrow i$, $kl \rightarrow j$, $c_{ijkl} \rightarrow C_{ij}$, Babuska & Cara 1991). The average of all rotated stiffness tensors is known as the Voigt-average C_{ij}^V. Accordingly, the average of all similarly rotated compliance tensors is called Reuss-average S_{ij}^R. The Voigt and Reuss averages represent the upper and lower bound, respectively, on the elastic properties of the polycrystalline aggregate. Assuming equal volume of each grain, C_{ij}^V and S_{ij}^R are

$$C_{ij}^V = \sum_{n=1}^{500} C_{ij}^n \frac{1}{500},$$
$$S_{ij}^R = \sum_{n=1}^{500} S_{ij}^n \frac{1}{500}. \quad (5)$$

The Voigt–Reuss–Hill (VRH) average (Hill 1952) is the intermediate value between C_{ij}^V and the inverted compliance tensor,

$$C_{ij}^R = \left(S_{ij}^R\right)^{-1}. \quad (6)$$

The VRH average thus provides a way to estimate the elastic constants of a textured polycrystal:

$$C_{ij}^{VRH} = \frac{1}{2}\left(C_{ij}^V + C_{ij}^R\right), \quad (7)$$

The elastic constants describe, together with the density, the velocity surface of the entire polycrystal and hence the seismic anisotropy (e.g. Kendall & Thomson 1989). This process defines a workflow to link salt deformation and associated seismic anisotropy in any salt deformation model. A full salt elasticity model generated, considering LPO-induced seismic anisotropy in the deformed salt sheet. The full elasticity model with the calculated seismic anisotropy is displayed in Fig. 10. The highest anisotropy is seen at the very top and bottom of the salt sheet. Strain analysis base is deformed primarily by shear, and the top part by compression (consistent with features observed in real salt bodies, e.g Rowan *et al.* 2001).

3.4 Seismic full wave-form modelling—synthetic VSP gather

The workflow outlined above provides us with a complex model of the anisotropy of the Mahogany salt body. In order to compare it with the shear wave splitting results, we need to interrogate the model in a way which reproduces the appropriate seismic phases. Thus, we simulate the propagation of seismic waves through the model using Specfem2D (Tromp *et al.* 2008), an open-source full wave form modelling software. Specfem2D uses the spectral-element method (e.g. Wang & Cai 2014). It has been used to simulate wave propagation in various complex media. Specfem2D supports seismic anisotropy, where the velocity is implemented by defining the elasticity and density of the medium. In total 6 s of wave propagation is modelled. The model geometry and wave field at different times is shown in Fig. 11. The snapshots are after 0.8, 1.7 and 5 s. The model geometry is based on the Mahogany salt deformation model and is similar to the field-data VSP setup. Mesh elements representing the salt are assigned with elasticities of the closest traced salt particle to each mesh element. The salt is surrounded by isotropic sediments with *P*-wave velocity of $VP_{Sediment} = 2500\,ms^{-1}$ and a shear velocity of $VS_{Sediment} = 1600\,ms^{-1}$. The receivers are at the bottom right of the salt body, and the first 10 receivers are inside the salt, imitating the geometry of the VSP-data setup. The synthetic wave-forms are used to estimate shear wave splitting, to compare the synthetic data with the VSP-field data set. As with the real data, shear wave splitting measurements are performed with SHEBA, by rotating the components into fast- and slow-direction, using the eigenvalue- and cross correlation method (e.g. Teanby *et al.* 2004). In Specfem2D no wave conversion from *P* to *SH* is possible, because the *P*—*SV* and *SH* wave trains are decoupled. We use SH-polarized and *SV*-polarized shear waves and compare the time delay between both components. Due to the anisotropy the *SH* and *SV* polarized waves propagate with different velocities through the salt, which leads to a time delay at the recording receivers between both waves. These lag times can be compared to the VSP data-set results, and

are shown in Fig. 12. The predicted delay time times are similar and show consistent results around 20 ms for both the synthetic- and field VSP data. The fast-direction cannot be inferred from the synthetic splitting data, because of the lack of *SH–SV* coupling in Specfem2D. We instead calculate the fast synthetic fast polarization directly from the anisotropic salt model from each set of effective elastic constants, assuming a density of $\rho = 2.16$ g cm^{-3}, using the Christoffel equation (e.g. Babuska & Cara 1991). We assume an incidence angle of 30° (measured from horizontal to ray direction) and an azimuth of 0°. The fast orientation is nearly horizontal in the direction of the flow, consistent with the VTI-observation in the VSP-field data.

4 DISCUSSION AND CONCLUSION

The VSP-field data shows clear evidence that the Mahogany salt body is, for the given geometry and acquisition, seismically anisotropic. The shear wave converted at the top of the salt shows a consistently higher delay time than the base converted shear wave. This delay time changes with receiver depth, which can be attributed to a longer travel path through the anisotropic salt, or possibly by a change in incidence angle with receiver depth.

We use texture plasticity modelling, together with a finite-element Mahogany salt sheet model to predict LPO induced seismic anisotropy, testing if a deformation-induced crystallographic halite fabric could explain the observed splitting. We generate a synthetic VSP data set from the resulting finite element model. Splitting from the field- and synthetic VSP show results agree remarkably well; the receivers with the best quality data showing similar delay times (∼20 ms) between the synthetic- and field VSP-data. The results strongly suggest that deformation induced LPO of halite can explain the splitting we observe associated with the Mahogany salt body. Despite more complexity in the real data, the fast shear wave polarization also shows a similar pattern, with SH leading SV.

The effect of strong anisotropy in the salt body could be profound. For example, seismic anisotropy can significantly affect seismic imaging. Alkhalifah *et al.* (1996) compared isotopic and VTI anisotropic depth images from a seismic survey from the African coast. Faults could be more clearly identified in the seismic image considering anisotropy. Our results showed an average delta parameter through the salt of about –0.06, which would lead in a zero-offset acquisition to a depth misfit of 6.2 per cent; for a 2-km-thick salt layer this is a misfit of 124 m.

Only dislocation plasticity is included in the VPSC modelling formulation, other recrystallization mechanisms are not included. Grain boundary migration tends to weaken LPO (Trimby *et al.* 2000) and is observed in wet salts (Urai & Spiers 2007). To investigate further how valid this assumption is, comparisons to natural rock salt textures are a possible future direction. Our texture modelling could also be improved by including other deformation mechanisms, apart from dislocation plasticity. The model is a 2-D deformation model, and a full 3-D model might give additional insights.

In this study only we have only considered seismic anisotropy due to lattice preferred orientation. In future, the derived strain models could be used to parametrize shape preferred orientation model, modelling deformed inclusions or deformed halite crystals. Here, inclusions of, for example water or sediment could be tested. Furthermore, mixed phases, such as anhydrite/halite mixtures, can be investigated instead of assuming only halite present in the rock salt. Anhydrite is highly anisotropic on crystal scale (e.g. Vargas-Meleza *et al.* 2015), which would increase the delay time in comparison to the modelled halite LPO shown in this work. Future work could consider modelling deformation texture of anhydrite and/or mixed halite/anhydrite phases. Moreover, the work flow we present here provides the potential to be to be used in an inverse sense to reconstruct the deformation history of specific salt structure from its contemporary seismic anisotropy pattern. Also, this work can be applied to other problems involving deforming crystalline solids, for example, understanding the deformation of glaciers.

ACKNOWLEDGEMENTS

This project has received funding from the European Union's Horizon 2020 research and innovation programme under the Marie Skłodowska-Curie grant agreement ('CREEP') No 642029. We thank Rockfield Global to make the collaboration possible and for the helpful advice in the model building process. We thank the members of the CREEP network for helpful discussions.

REFERENCES

Alkhalifah, T., Tsvankin, I., Larner, K. & Toldi, J., 1996. Velocity analysis and imaging in transversely isotropic media: methodology and a case study, *Leading Edge,* **15**(5), 371–378.

Babuska, V. & Cara, M., 1991. *Seismic Anisotropy in the Earth,* Vol. **10,** Springer.

Camp, W.K., 1998. Geologic model and reservoir description of the deepwater "P and S" at subsalt Mahogany field, Gulf of Mexico, in *Paper presented at Hedberg Conference on Integration of Geologic Models for Understanding Risk in the Gulf of Mexico,* Cairo, Eygpt.

Carter, N.L. & Hansen, F.D., 1983. Creep of rocksalt, *Tectonophysics,* **92**(4), 275–333.

Christie, P., Hughes, V. & Kennett, B., 1983. Velocity filtering of seismic reflection data, *First Break,* **1**(3), 9–24.

Crook, A., Willson, S., Yu, J. & Owen, D., 2006. Predictive modelling of structure evolution in sandbox experiments, *J. Struct. Geol.,* **28**(5), 729–744.

Dribus, J.R., Jackson, M.P., Kapoor, J. & Smith, M.F., 2008. The prize beneath the salt, *Oilfield Rev.,* **15,** 4–17.

Eshelby, J.D., 1957. The determination of the elastic field of an ellipsoidal inclusion, and related problems, *Proc. R. Soc. Lond., A,* **241**(1226), 376–396.

Firme, P., Roehl, D., Romanel, C., Poiate, E.Jr & Costa, A., 2015. Multimechanism deformation creep model applied to Brazilian salt rocks: PALP Firme D. Roehl, in *Mechanical Behaviour of Salt VIII,* pp. 351–358, CRC Press.

Fredrich, J., Fossum, A. & Hickman, R., 2007. Mineralogy of deepwater Gulf of Mexico salt formations and implications for constitutive behaviour, *J. Petrol. Sci. Eng.,* **57**(3–4), 354–374.

Gebrande, H., 1982. Elastic wave velocities and constants of elasticity of rocks at room temperature and pressures up to 1 GPa, *Phys. Propert. Rocks,* **1,** 35–99.

Hale, D., Hill, N.R. & Stefani, J., 1992. Imaging salt with turning seismic waves, *Geophysics,* **57**(11), 1453–1462.

Harrison, H., Moore, D. & Hodgkins, P., 2010. A geologic review of the Mahogany subsalt discovery: a well that proved a play (The Mahogany subsalt discovery: a unique hydrocarbon play, of shore Louisiana), in *AAPG Annual Conference & Exhibition*.

Heege, J.T., Bresser, J.D. & Spiers, C., 2005. Rheological behaviour of synthetic rocksalt: the interplay between water, dynamic recrystallization and deformation mechanisms, *J. Struct. Geol.,* **27**(6), 948–963.

Heidari, M., Nikolinakou, M.A., Hudec, M.R. & Flemings, P.B., 2016. Geomechanical analysis of a welding salt layer and its effects on adjacent sediments, *Tectonophysics,* **683,** 172–181.

Helffrich, G., Wookey, J. & Bastow, I., 2013. *The Seismic Analysis Code: A Primer and User's Guide,* Cambridge Univ. Press.

Hess, H., 1964. Seismic anisotropy of the uppermost mantle under oceans, *Nature,* **203**(4945), 629.

Hill, R., 1952. The elastic behaviour of a crystalline aggregate, *Proc. Phys. Soc., A,* **65**(5), 349.

Hosford, W.F., 2010. *Mechanical Behaviour of Materials,* Cambridge Univ. Press.

Hudec, M.R. & Jackson, M.P., 2007. Terra infirma: understanding salt tectonics, *Earth-Sci. Rev.,* **82**(1–2), 1–28.

Jackson, C.A.-L. & Lewis, M.M., 2012. Origin of an anhydrite sheath encircling a salt diapir and implications for the seismic imaging of steep-sided salt structures, Egersund basin, northern North Sea, *J. Geol. Soc.,* **169**(5), 593–599.

Jones, I. & Davison, I., (2014) Seismic Imaging in an around salt bodies *Interpretation,* **2**(4), doi.org/10.1190/INT-2014-0033.1, 2324-8858.

Kendall, J. & Thomson, C., 1989. A comment on the form of the geometrical spreading equations, with some numerical examples of seismic ray tracing in inhomogeneous, anisotropic media, *Geophys. J. Int.,* **99**(2), 401–413.

Kendall, R.R., Gray, S.H. & Murphy, G.E., 1998. Subsalt imaging using prestack depth migration of converted waves: Mahogany field, Gulf of Mexico, in *SEG Technical Program Expanded Abstracts 1998,* pp. 2052–2055, Society of Exploration Geophysicists.

Lafond, C., Jones, I.F., Bridson, M., Houllevigue, H., Kerdraon, Y. & Peliganga, J., 2003. Imaging deepwater salt bodies in West Africa, *Leading Edge,* **22**(9), 893–896.

Lebensohn, R. & Tomé, C., 1993. A self-consistent anisotropic approach for the simulation of plastic deformation and texture development of polycrystals: application to zirconium alloys, *Acta Metall. Mater.,* **41**(9), 2611–2624.

Lebensohn, R.A., Dawson, P.R., Kern, H.M. & Wenk, H.-R., 2003. Heterogeneous deformation and texture development in halite polycrystals: comparison of different modelling approaches and experimental data, *Tectonophysics,* **370**(1), 287–311.

Munson, B.R., Okiishi, T.H., Huebsch, W.W. & Rothmayer, A.P., 2013. *Fluid Mechanics,* Wiley.

Munson, D.E. & Dawson, P., 1979. Constitutive model for the low temperature creep of salt (with application to WIPP), Tech. rep., Sandia Laboratories, United States.

Munson, D.E. *et al.*, 2004. MD constitutive model parameters defined for gulf coast salt domes and structures, in *Gulf Rocks 2004, the 6th North America Rock Mechanics Symposium (NARMS),* American Rock Mechanics Association.

Nygaard, R., Gutierrez, M., Bratli, R.K. & Hoeg, K., 2006. Brittle - ductile transition, shear failure and leakage in shales and mudrocks, *Mar. Petrol. Geol.,* **23,** 201–212.

Perić, D. & Crook, A., 2004. Computational strategies for predictive geology with reference to salt tectonics, *Comp. Methods Appl. Mech. Eng.,* **193**(48–51), 5195–5222.

Picard, D., Dimanov, A. & Raphanel, J., 2018. Plastic behavior of halite single-crystals at different temperatures and strain rates: New insights from in-situ experiments and full field measures, *Mater. Sci. Eng., A,* **732,** 284–297.

Planchart, C., 2014. Estimation of salt anisotropy using zero offset, walk away and walk around VSP data from the Red Sea, Saudi Arabia: a case study, in *SEG Technical Program Expanded Abstracts,* pp. 389–393, Society of Exploration Geophysicists.

Ranganathan, S.I. & Ostoja-Starzewski, M., 2008. Universal elastic anisotropy index, *Phy. Rev. Lett.,* **101**(5), 055504.

Raymer, D., Kendall, J., Pedlar, D., Kendall, R., Mueller, M. & Beaudoin, G., 2000a. The significance of salt anisotropy in seismic imaging, in *SEG Technical Program Expanded Abstracts 2000,* pp. 562–565, Society of Exploration Geophysicists.

Raymer, D.G., Tommasi, A. & Kendall, J.-M., 2000b. Predicting the seismic implications of salt anisotropy using numerical simulations of halite deformation, *Geophysics,* **65**(4), 1272–1280.

Rockfield Software Ltd, 2013. ELFEN Forward Modelling Manual.

Rowan, M.G., Ratliff, R.A., Trudgill, B.D. & Duarte, J.B., 2001. Emplacement and evolution of the Mahogany salt body, central Louisiana outer shelf, northern Gulf of Mexico, *AAPG Bull.,* **85**(6), 947–969.

Sheriff, R.E. & Geldart, L.P., 1995. *Exploration Seismology,* Cambridge Univ. Press.

Silver, P.G. & Chan, W.W., 1991. Shear wave splitting and subcontinental mantle deformation, *J. geophys. Res.,* **96**(B10), 16429–16454.

Teanby, N., Kendall, J.-M. & Van der Baan, M., 2004. Automation of shear-wave splitting measurements using cluster analysis, *Bull. seism. Soc. Am.,* **94**(2), 453–463.

Thigpen, J.R., Roberts, D., Snow, J.K., Walker, C.D. & Bere, A., 2019. Integrating kinematic restoration and forward finite element simulations to constrain the evolution of salt diapirism and overburden deformation in evaporite basins, *J. Struct. Geol.,* **118,** 68–86.

Thomsen, L., 1986. Weak elastic anisotropy, *Geophysics,* **51**(10), doi.org/10.1190/1.1442051, 0016-8033 .

Tommasi, A., Mainprice, D., Canova, G. & Chastel, Y., 2000. Viscoplastic self-consistent and equilibrium-based modeling of olivine lattice preferred orientations: implications for the upper mantle seismic anisotropy, *J. geophys. Res.,* **105**(B4), 7893–7908.

Tomé, C., Lebensohn, R. & Kocks, U., 1991. A model for texture development dominated by deformation twinning: application to zirconium alloys, *Acta Metall. Mater.,* **39**(11), 2667–2680.

Trimby, P.W., Drury, M.R. & Spiers, C.J., 2000. Recognising the crystallographic signature of recrystallisation processes in deformed rocks: a study of experimentally deformed rocksalt, *J. Struct. Geol.,* **22**(11–12), 1609–1620.

Tromp, J., Komattisch, D. & Liu, Q., 2008. Spectral-element and adjoint methods in seismology, *Commun. Comput. Phys.,* **3**(1), 1–32.

Urai, J. & Spiers, C., 2007. The effect of grain boundary water on deformation mechanisms and rheology of rocksalt during long-term deformation, in *Proceedings of the Sixth Conference on the Mechanical Behavior of Salt,* 'SaltMech6', Hannover, Germany, 22–25 May 2007, pp. 149–158.

Van Keken, P., Spiers, C., Van den Berg, A. & Muyzert, E., 1993. The effective viscosity of rocksalt: implementation of steady-state creep laws in numerical models of salt diapirism, *Tectonophysics,* **225**(4), 457–476.

Vargas-Meleza, L., Healy, D., Alsop, G.I. & Timms, N.E., 2015. Exploring the relative contribution of mineralogy and CPO to the seismic velocity anisotropy of evaporites, *J. Struct. Geol.,* **70,** 39–55.

Walker, A., Forte, A., Wookey, J., Nowacki, A. & Kendall, J.-M., 2011. Elastic anisotropy of D" predicted from global models of mantle flow, *Geochem. Geophys. Geosyst.,* **12**(10), doi:10.1029/2011GC003732.

Wang, X. & Cai, M., 2014. Wave propagation simulation in underground mines by Specfem2D, in *Proceedings of the Seventh International Conference on Deep and High Stress Mining,* 723–738, Australian Centre for Geomechanics.

Weimer, P., Rowan, M.G., McBride, B.C. & Kligfield, R., 1998. Evaluating the petroleum systems of the northern deep Gulf of Mexico through integrated basin analysis: an overview, *AAPG Bull.,* **82**(5), 865–877.

Wenk, H., Canova, G., Molinari, A. & Mecking, H., 1989. Texture development in halite: comparison of Taylor model and self-consistent theory, *Acta Metall.,* **37**(7), 2017–2029.

Wenk, H.-R., Armann, M., Burlini, L., Kunze, K. & Bortolotti, M., 2009. Large strain shearing of halite: experimental and theoretical evidence for dynamic texture changes, *Earth planet. Sci. Lett.,* **280**(1), 205–210.

Wood, D.M., 1990. *Soil Behaviour and Critical State Soil Mechanics,* Cambridge Univ. Press.

Wuestefeld, A., Al-Harrasi, O., Verdon, J.P., Wookey, J. & Kendall, J.-M., 2010. A strategy for automated analysis of passive microseismic data to image seismic anisotropy and fracture characteristics, *Geophys. Prospect.,* **58**(5), 755–773.

Wuestefeld, A. & Bokelmann, G., 2007. Null detection in shear-wave splitting measurements, *Bull. seism. Soc. Am.,* **97**(4), 1204–1211.

Zong, J., Stewart, R. & Dyaur, N., 2014. Salt anisotropy: ultrasonic lab experiments and traveltime ramifications, *SEG Technical Program Expanded Abstracts 2014,* pp. 383–388.

APPENDIX

A1 Multimechanism Deformation (MD) constitutive model

We follow Munson & Dawson (1979), Munson *et al.* (2004) and Fredrich *et al.* (2007) to describe the Multimechanism creep model. The MD-model is a mathematical formulation, describing the mechanical behaviour of various rock salts. Depending on stress/temperature is has been shown that different rock salt deformation mechanism are active, controlling the creep behaviour of rock salt (Munson & Dawson 1979). The MD-model considers dislocations climb active at high temperatures and low stresses, dislocation slip at high stresses and a third undefined mechanism at low temperatures and low stresses, which is experimentally well characterized (Fredrich *et al.* 2007). The steady state creep rates for the three mechanisms described are:

$$\dot{\varepsilon}_{s1} = A_1 e^{-Q_1/RT}\left(\frac{\sigma}{G}\right)^{n_1}, \tag{A1}$$

$$\dot{\varepsilon}_{s2} = A_2 e^{-Q_2/RT}\left(\frac{\sigma}{G}\right)^{n_2}, \tag{A2}$$

$$\dot{\varepsilon}_{s3} = H(\sigma-\sigma_0)\left(B_1 e^{\frac{-Q_1}{RT}} + B_2 e^{\frac{-Q_2}{RT}}\right)\sinh\left(\frac{q}{G}(\sigma-\sigma_0)\right). \tag{A3}$$

The subscripts refer to the different mechanisms, where $\dot{\varepsilon}_{s_1}$ is the strain rate contributed by dislocation climb, $\dot{\varepsilon}_{s_2}$ by the undefined mechanism and $\dot{\varepsilon}_{s_3}$ by dislocation glide. $A_{1,2}$ and $B_{1,2}$ are constant, Q is the activation energy, T is the absolute temperature. We assume a temperature gradient of 35 K km^{-1} and a surface temperature of 10 °C. G is the shear modulus, $n_{1,2}$ are stress exponents, q is a stress constant. The contribution of $\dot{\varepsilon}_{s3}$ is limited by a Heaviside function H with argument $\sigma - \sigma_0$, where σ_0 is a reference stress of this mechanism. The Heaviside function is equal to 1 if the argument is positive ($\sigma > \sigma_0$) and is zero if the argument is negative ($\sigma < \sigma_0$). R is the universal Gas constant and σ describes the equivalent stress, given in the Tresca Form:

$$\sigma = |\sigma_1 - \sigma_3|. \tag{A4}$$

All the mechanisms act at the same time. The total steady-state creep rate is therefore the sum over all steady-state creep rates:

$$\dot{\varepsilon_s} = \dot{\varepsilon}_{s_1} + \dot{\varepsilon}_{s_2} + \dot{\varepsilon}_{s_3}. \tag{A5}$$

A multiplier F relates the equivalent strain rate $\dot{\varepsilon}_{eq}$ to the steady-state creep rate $\dot{\varepsilon}_s$:

$$\dot{\varepsilon}_{eq} = F\,\dot{\varepsilon}_s. \tag{A6}$$

F is a function representing transient creep behaviour. It includes a work-hardening branch, an equilibrium branch, and a recovery branch:

$$F = \begin{cases} \exp\left(\Delta\left(1-\frac{\zeta}{\varepsilon_t^*}\right)^2\right) & \text{if } \zeta < \varepsilon_t^* \\ 1 & \text{if } \zeta = \varepsilon_t^* \\ \exp\left(-\delta\left(1-\frac{\zeta}{\varepsilon_t^*}\right)^2\right) & \text{if } \zeta > \varepsilon_t^* \end{cases}, \tag{A7}$$

where Δ, is the work-hardening parameter and δ is the recovery parameter, ζ is the hardening variable and ε_t^* is the transient strain limit. The curvature is defined by Δ, or δ, depending on whether the transient is work-hardening or recovering. The transient limit is defined by

$$\varepsilon_t^* = K_0 e^{cT}\left(\frac{\sigma}{G}\right)^m, \tag{A8}$$

where K_0, c and m are constants. The evolution of the kinematic hardening parameter is given by

$$\dot{\zeta} = \left(F-1\right)\dot{\varepsilon}_s, \tag{A9}$$

which approaches zero when the steady-state condition is achieved.

The different model parameters need to be found by a fitting routine. Fredrich *et al.* (2007) constrain the constitutive response of deepwater Gulf of Mexico salt diapirs from different regions. The expected constitutive behaviour of all rock salt samples lies within the range of well characterized Gulf of Mexico domal salts. The best estimates to the constitutive behaviour of Gulf of Mexico rock salts, according to Fredrich *et al.* (2007), are taken in this study and are shown in Table A1. Those parameters are used to model the salt rheology in the Mahogany salt sheet model. Linear elastic parameters of the Gulf of Mexico salt assumed are a Youngs Modulus of $E = 31$GPa and a Poisson's-ratio of $\nu = 0.4$, chosen according to Heidari *et al.* (2016).

In the current model we only use the steady state form of the described law, which means no transient creep is considered and we only incorporate mechanisms 1 and 2 (equation 8 and 9). The Heaviside function in equation 10 has an argument of $\sigma = 20.57$ MPa (see table 2). It is unlikely that over geological timescales salt experiences such large differential stress. For completeness, we described the whole MD-constitutive model.

A2 SR3 constitutive model

The rheology of the sediments are modelled using the SR3 material model. The SR3 material model is a constitutive critical-state poroelastic-plastic material model, based on the 'cam clay' material model concept (Wood 1990). A full description of the SR3-material model can be found in Crook *et al.* (2006). An important factor of this model is that takes into account material inelastic behaviour (Wood 1990). The yield surface. The yield surface is a three-invariant surface and is defined as:

$$\phi(\sigma, \varepsilon_v^p) = g(\theta, p)q + (p - p_t)\tan\beta\left(\frac{p-p_c}{p_t-p_c}\right)^{\frac{1}{n}}, \tag{A10}$$

where θ is the Lode angle, which can be considered as a measure of loading type (Crook *et al.* 2006), p is the effective mean stress, q is the deviatoric stress, p_t is the tensile intercept, p_c is the compressive intersect, β and n are material constants defining the shape of the yield surface in $p - q$ plane and $g(\theta, p)$ is a function controlling the shape of the yield surface in the deviatoric plane. The material hardening is defined as:

$$p_c = p_{c0}\exp\left[\frac{\upsilon\varepsilon_v^p}{\lambda-\kappa}\right], \tag{A11}$$

$$p_t = p_{t0}\exp\left[\frac{\upsilon(\varepsilon_v^p)_{max}}{\lambda-\kappa}\right] \tag{A12}$$

where v is the specific volume, and λ and κ are the slopes of the normal compression line and unloading-reloading lines; $(\varepsilon_v^p)_{\max}$ is the maximum dilatational volumetric plastic strain. The plastic strain rate is defined as:

$$\dot{\varepsilon}^p = \dot{\lambda}\frac{d\Psi}{d\sigma} \tag{A13}$$

Table A1. MD model parameters used in the Mahogany salt body salt sheet model.

G [GPa]	A_1 [s^{-1}]	Q_1 [Kcal mol^{-1}]	n_1	B_1 [s^{-1}]
12.4	5.954e22	25	5.5	4.321e6
A_2 [s^{-1}]	**Q_2** [Kcal mol^{-1}]	**n_2**	**B_2 [s^{-1}]**	**σ_0** [MPa]
6.869e12	10	5.0	2.154e-2	20.57
q	**R [cal/mol − deg]**	**m**	**K_0**	**c [T^{-1}]**
5.335e3	1.987	3	1.342e6	9.198e-3

Table A2. SR3 modelling parameters used for the calculation, according to Nygaard *et al.* (2006) and Rockfield Software ltd (2013).

E [MPa]	ν	K_0 [MPa]	κ	p_t^0 [MPa]	p_c^0 [MPa]	
40	0.25	10	0.01	0.085	−1	
β[°]	**ψ[°]**	**β_0**	**β_0[MPa^{-1}]**	**α**	**N**	**n**
60	51	0.6	0.725	0.25	1.3	0.38

where Ψ is the plastic potential defined as:

$$\Psi(p, \varepsilon_v^p) = g(\theta, p)q + (p - p_t)\tan\psi\left(\frac{p - p_c}{p_t - p_c}\right)^{\frac{1}{n}} \tag{A14}$$

where ψ is a material parameter and dilation angle, $\dot{\lambda}$ is a plastic multiplier. The deviatoric correction term $g(\theta, p)$ is defined as:

$$g(\theta, p) = \left[\frac{1}{1 - \beta^{\pi}(p)}\left(1 + \beta^{\pi}(p)\frac{r^3}{q^3}\right)\right]^{N^{\pi}}, \tag{A15}$$

N^{π} is a material constant, and β^{π} is a function of p:

$$\beta^{\pi}(p) = \beta_0^{\pi} exp\left(\beta_1^{\pi} p\frac{p_c}{p_c^0}\right), \tag{A16}$$

β_0^{π} and β_1^{π} are material constants, p_c^0 and p_c is the initial and current pre-consolidation pressure.

The values used for in the SR3 material model are listed in Table A2. Those values have been successfully used to model sediment rheology around rock salt in, for example Heidari *et al.* (2016).